*coatings*

Article

# Ultrathin $Al_2O_3$ Coating on $LiNi_{0.8}Co_{0.1}Mn_{0.1}O_2$ Cathode Material for Enhanced Cycleability at Extended Voltage Ranges

**Wenchang Zhu [1,2], Xue Huang [1,2], Tingting Liu [3], Zhiqiang Xie [4], Ying Wang [4], Kai Tian [1,2], Liangming Bu [1,2], Haibo Wang [1,2,5], Lijun Gao [1,2,*] and Jianqing Zhao [1,2,*]**

[1] College of Energy, Soochow Institute for Energy and Materials InnovationS, Soochow University, Suzhou 215006, China; 20164208119@stu.suda.edu.cn (W.Z.); 20174208074@stu.suda.edu.cn (X.H.); 20174208072@stu.suda.edu.cn (K.T.); 20164208112@stu.suda.edu.cn (L.B.); wanghb@suda.edu.cn (H.W.)
[2] Key Laboratory of Advanced Carbon Materials and Wearable Energy Technologies of Jiangsu Province, Soochow University, Suzhou 215006, China
[3] Suzhou University of Science and Technology & Jiangsu Key Laboratory of Environmental Science and Engineering, Suzhou 215001, China; liutt@mail.usts.edu.cn
[4] Department of Mechanical & Industrial Engineering, Louisiana State University, Baton Rouge, LA 70803, USA; zxie5@lsu.edu (Z.X.); ywang@lsu.edu (Y.W.)
[5] Institute of Chemical Power Sources, Soochow University, Suzhou 215600, China
* Correspondence: gaolijun@suda.edu.cn (L.G.); jqzhao@suda.edu.cn (J.Z.); Tel.: +86-512-6522-9905 (L.G. & J.Z.)

Received: 20 December 2018; Accepted: 31 January 2019; Published: 3 February 2019

**Abstract:** Ni-rich $LiNi_{0.8}Co_{0.1}Mn_{0.1}O_2$ oxide has been modified by ultrathin $Al_2O_3$ coatings via atomic layer deposition (ALD) at a growth rate of 1.12 Å/cycle. All characterizations results including TEM, SEM, XRD and XPS together confirm high conformality and uniformity of the resultant $Al_2O_3$ layer on the surface of $LiNi_{0.8}Co_{0.1}Mn_{0.1}O_2$ particles. Coating thickness of the $Al_2O_3$ layer is optimized at ~2 nm, corresponding to 20 ALD cycles to enhance the electrochemical performance of Ni-rich cathode materials at extended voltage ranges. As a result, 20 $Al_2O_3$ ALD-coated $LiNi_{0.8}Co_{0.1}Mn_{0.1}O_2$ cathode material can deliver an initial discharge capacity of 212.8 mAh/g, and an associated coulombic efficiency of 84.0% at 0.1 C in a broad voltage range of 2.7–4.6 V vs. $Li^+/Li$ in the first cycle, which were both higher than 198.2 mAh/g and 76.1% of the pristine $LiNi_{0.8}Co_{0.1}Mn_{0.1}O_2$ without the $Al_2O_3$ protection. Comparative differential capacity ($dQ/dV$) profiles and electrochemical impedance spectra (EIS) recorded in the first and 100th cycles indicated significant $Al_2O_3$ ALD coating effects on suppressing phase transitions and electrochemical polarity of the Ni-rich $LiNi_{0.8}Co_{0.1}Mn_{0.1}O_2$ core during reversible lithiation/delithiation. This work offers oxide-based surface modifications with precise thickness control at an atomic level for enhanced electrochemical performance of Ni-rich cathode materials at extended voltage ranges.

**Keywords:** $Al_2O_3$ oxide; atomic layered deposition; $LiNi_{0.8}Co_{0.1}Mn_{0.1}O_2$; Ni-rich cathode material; lithium ion battery

## 1. Introduction

Lithium ion batteries have been dominantly applied in hybrid electric vehicles (HEVs) and pure electric vehicles (EVs) [1,2], which significantly enhances our living environment. In particular for electric transportation systems and future large-scale applications of stationary grid energy storage, lithium ion batteries are required to provide higher energy and power densities, together with excellent long-term service life and acceptable cost [3]. Performance of lithium ion batteries critically depends on the electrochemical properties and behaviors of electrode materials both in cathodes and anodes [4–6]. Because of the rapid development of practical Si–C composite anode materials, developing high-performance cathode materials with high specific capacity, high working potential, excellent cycle life, reliable safety, and low cost has become an urgent requirement [7–9]. Li-excess and Ni-rich layered oxides have been extensively investigated as high-energy cathode materials for superior lithium ion batteries [10,11]. Despite delivering an attractive discharge capacity of ~250 mAh/g, Li-excess layered cathode materials have been suffering from two crucial issues. One is the layered-to-spinel phase transition during prolonged electrochemical cycles, leading to continuous voltage fading. The other is low coulombic efficiency in the first cycle that results from the initial electrochemical activation of the $Li^+$-inactive $Li_2MnO_3$ component [10,12,13]. These two problems impede practical applications of Li-excess cathode materials. Alternatively, Ni-rich layered oxides have been considered as feasible cathode materials by offering a reversible capacity of ~200 mAh/g and a stable working voltage at ~3.8 V vs. $Li^+/Li$.

It is well-known that the resultant electrochemical performance of Ni-rich cathode materials is essentially determined on the specific composition of Ni, Co, and Mn elements within these ternary transition metal oxides, $LiNi_{1-x-y}Co_xMn_yO_2$ ($x + y < 0.5$) [11,14,15]. Higher Ni content results in higher lithium storage capacity of $LiNi_{1-x-y}Co_xMn_yO_2$, but leads to the undesired formation of $Li^+/Ni^{2+}$ cation mixing in the layered structure; the expense of safety in material usage and more complexity in the material preparation [16,17]. Mn and Co dopants have been demonstrated to enhance the structural robustness and cationic ordering for $LiNi_{1-x-y}Co_xMn_yO_2$ variants, respectively. However, the specific capacity has to be sacrificed, when Mn and Co contents are increased. In order to rapidly promote practical applications of Ni-rich cathode materials for superior lithium ion batteries, poor cycling and thermal stabilities of $LiNi_{1-x-y}Co_xMn_yO_2$ should be urgently addressed, especially for materials with high Ni content. Capacity fading can be exacerbated, when these Ni-rich $LiNi_{1-x-y}Co_xMn_yO_2$ cathodes are cycled at broad voltage ranges with a high upper cut-off voltage above 4.3 V vs. $Li^+/Li$. One reason is that the intensive oxidation capability of $Ni^{3+/4+}$ redox could aggravate parasitic side reactions during lithiation/delithiation of $LiNi_{1-x-y}Co_xMn_yO_2$ cathode materials, leading to undesired electrolyte decomposition and solid electrolyte interphase (SEI) formation at the surface of the cathode. The other reason is the induced phase transition from the initial layered structure to spinel-like and/or NiO-like rock-salt phases at the surface of $LiNi_{1-x-y}Co_xMn_yO_2$ particles, because the formation of $Li^+$ vacancies in high concentration at deep charge destabilizes the initial layered structure of $LiNi_{1-x-y}Co_xMn_yO_2$ [18]. These unfavorable structural transformations are consecutive, and gradually overspread from the surface to bulk Ni-rich layered oxides [17,19]. In addition, the formation of impure phases definitely brings about structural degradation and increased kinetic barrier for lithium ion diffusion, causing capacity fading and inferior rate capability of $LiNi_{1-x-y}Co_xMn_yO_2$ cathode materials [20,21].

Surface modifications, either on particles of active cathode materials or at the surface of the entire cathode, have been demonstrated to improve electrochemical performance for various cathode materials even in harsh operation conditions, such as elevated working temperatures and broad voltage ranges [22,23]. Oxides are considered common coating materials, because of their low material cost, simple synthetic procedure, and high effectiveness in protecting internal electrode materials. Various examples have been reported in the literature [24–28], involving $Al_2O_3$, $ZrO_2$, ZnO, $TiO_2$, $Cr_2O_3$, $SnO_2$, etc. However, associated electrochemical performance of modified cathode materials is sensitively determined by qualities of the coated oxides in terms of thickness, conformality, uniformity, and integrity. Oxide coatings prepared by atomic layer deposition (ALD) have been demonstrated to considerably enhance electrochemical performance for various cathode materials, involving layered $LiCoO_2$ [29,30], spinel $LiMn_2O_4$, and $LiMn_{1.5}Ni_{0.5}O_4$ [31,32]; Ni-rich $LiNi_{1-x-y}Co_xMn_yO_2$ and $LiNi_{0.8}Co_{0.15}Al_{0.05}O_2$ [33,34]; and Li-excess $Li[Li_{1-x}M_x]O_2$ oxides [35]. The ALD technique can result in highly conformational and uniform oxide coating layers at the entire surface of the underlying substrates, and thus has been considered as an effective method for surface modifications of different cathode materials. Ni-rich cathode materials have been dominantly used for lithium ion batteries to power currently-developed electric automobiles, but still suffer from poor service life, especially in harsh operation conditions, such as at elevated working temperatures and/or in extended voltage ranges. As reported in the literature [33,34], $Al_2O_3$ ALD coatings contribute to enhanced cycling stabilities of $LiNi_{0.5}Co_{0.2}Mn_{0.3}O_2$, $LiNi_{0.8}Co_{0.1}Mn_{0.1}O_2$, and $LiNi_{0.8}Co_{0.15}Al_{0.05}O_2$ by protecting coated Ni-rich oxide particles from parasitic side reactions at the cathode's surface. However, the insulating property of $Al_2O_3$ material makes it is necessary to precisely control the coating's thickness, in order to maximize the electrochemical performance of Ni-rich cathode materials. In addition, it is also urgent to understand structural features and chemical environments between oxide coatings and Ni-rich oxide particles.

The ALD technique was employed in this work to coat ultrathin $Al_2O_3$ onto Ni-rich $LiNi_{0.8}Co_{0.1}Mn_{0.1}O_2$ target material (marked as $n$ $Al_2O_3$ ALD NCM811, then responses to the number of ALD cycles related to the thickness control of $Al_2O_3$ coating layer). TEM observations were used to examine the structural characteristics of resultant $Al_2O_3$ coatings and determine the ALD growth rate of $Al_2O_3$ oxide. XPS spectra were used to study chemical environments of different $n$ $Al_2O_3$ ALD NCM811 ($n$ = 10, 20 and 50) materials. Electrochemical performance of three $n$ $Al_2O_3$ ALD NCM811 cathode materials were evaluated and compared with the bare NCM811 cathode in a broad voltage range of 2.7–4.6 V vs. $Li^+/Li$. This work offers a high-quality oxide coating for Ni-rich cathode materials by using the ALD method, which significantly contributes to improved electrochemical performance in extended voltage ranges for superior lithium ion batteries.

## 2. Materials and Methods

### 2.1. Synthesis of Ni-Rich Layered $LiNi_{0.8}Co_{0.1}Mn_{0.1}O_2$ Material

In a typical sol (solution)-gel route, stoichiometric amounts of $CH_3COOLi\cdot 2H_2O$, $Ni(CH_3COO)_2\cdot 4H_2O$, $Co(CH_3COO)_2\cdot 4H_2O$, and $Mn(CH_3COO)_2\cdot 4H_2O$ were dissolved in 50 mL of distilled water. An extra 3 mol.% of the lithium source was used to compensate for the volatilization of lithium at high heating temperatures. The green sol was obtained after the solvent was completely evaporated, and was then transferred to dry in vacuum at 120 °C for 12 h. Dried gel heat treatments were carried out at 850 °C for 5 h, under pure $O_2$ flow at a temperature ramp of 5 °C/min. The resultant black $LiNi_{0.8}Mn_{0.1}Co_{0.1}O_2$ (marked as NCM811) powder was collected after cooling to room temperature.

### 2.2. $Al_2O_3$ Coating on $LiNi_{0.8}Co_{0.1}Mn_{0.1}O_2$ Particles Through Atomic Layer Deposition

The atomic layer deposition of $Al_2O_3$ coating on $LiNi_{0.8}Co_{0.1}Mn_{0.1}O_2$ particles was performed in a Savannah 100 ALD system (Cambridge NanoTech Inc., Waltham, MA, USA) at 120 °C, by applying $Al(CH_3)_3$ (Trimethylalumium, TMA) and $H_2O$ as precursors with exposure time of 0.01 s, waiting time of 5 s, and purge time of 40 s, respectively. Nitrogen gas was used as the flow gas, and the flow rate was set at 20 sccm. The vacuum condition in the reaction chamber was controlled at $10^{-3}$–$10^{-2}$ torr, and the overpressure threshold for the coating processes was set at 250 torr. Two self-terminating reactions involved in the ALD growth of $Al_2O_3$ layer are described as follows:

$$\text{AlOH}^* + \text{Al(CH}_3)_3 \rightarrow \text{Al-O-Al-(CH}_3)_2{}^* + \text{CH}_4 \tag{1}$$

$$\text{Al-CH}_3{}^* + \text{H}_2\text{O} \rightarrow \text{AlOH}^* + \text{CH}_4 \tag{2}$$

$LiNi_{0.8}Co_{0.1}Mn_{0.1}O_2$ particles coated with the $Al_2O_3$ layer under different ALD cycles were marked as $n$ $Al_2O_3$ ALD NCM811 (the n corresponds to the number of ALD cycles).

### 2.3. Characterizations

Crystallographic structures of bare NCM811 and $Al_2O_3$-coated NCM811 materials were examined by X-ray diffraction (XRD), using a Bruker D8 Advance automatic diffractometer (Bruker, Billerica, MA, USA) with Cu Kα radiation. Morphologies and energy dispersive spectroscopic (EDS) mappings of different samples were observed by field emission scanning electron microscopy (FESEM) on a Hitachi SU-8010 (Hitachi High-Tech Corp., Tokyo, Japan) and FEI Quanta FEG 250 microscopies (FEI, Hillsboro, OR, USA), respectively, with an acceleration voltage at 15/20 kV in a secondary electrons (SE) detection mode. The Everhart Thornley Detector (ETD) was used to collected electron signals. Detailed structural features of different specimens were captured by transmission electron microscopy (TEM) and high-resolution transmission electron microscopy (HRTEM) coupled with selected area electron diffraction (SAED) on a FEI Tecnai G2 T20 equipment (FEI, Hillsboro, OR, USA), at an acceleration voltage of 200 kV. Chemical environments and valent states of cations within different materials were characterized by X-ray photoelectron spectroscopic (XPS) measurements on an ESCALAB 250Xi XPS device (Thermo Fisher Scientific, Waltham, MA USA). All XPS spectra were calibrated according to the binding energy of the C 1*s* peak at 284.6 eV.

### 2.4. Electrochemical Measurements

The working electrodes were composed of 80 wt.% active cathode materials, 10 wt.% super p as the conductive carbon, and 10 wt.% polyvinylidenefluoride (PVDF) as the binder. These cathodes were assembled into two-electrode CR2025-type coin cells (Shenzhen Kejing Star Technology Co., LTD., Shenzhen, China), in an Ar-filled glove box (MBraun, Garching, Germany) for electrochemical measurements, with the metallic lithium foil as the reference, and counter electrodes with the glass microfiber (Whatman, Grade GF/B, Little Chalfont, UK) as the separator. The electrolyte was a 1 M $LiPF_6$ solution dissolved in ethylene carbonate (EC) and dimethyl carbonate (DMC) at a volumetric ratio of 1:1. The real loading of active material was ~3.5 mg in the cathode with a diameter of 12 mm and a thickness of ~50 mm for all electrode materials. The electrolyte volume used during the coin cell assembly was ~0.5 mL per unit. Galvanostatic charge and discharge were performed at different current densities in a voltage range of 2.7–4.6 V vs. $Li^+/Li$ on a LAND battery testing system (Jinnuo, Wuhan, China). The current density corresponding to 1 C was 200 mA/g. Electrochemical impedance spectroscopy (EIS) was conducted in a frequency range of 10 mHz–100 kHz with an AC amplitude of 5 mV on the Autolab electrochemical workstation (PGSTAT302N, Metrohm Autolab, Utrecht, The Netherlands).

## 3. Results and Discussion

### 3.1. Characteristics of $Al_2O_3$ Layer Deposited on NCM811 Particles via ALD Coating

As shown in the schematic illustrations in Figure 1a, the ALD growth of $Al_2O_3$ coating at the surface of NCM811 particles was subjected to a sequence of chemisorption and self-terminating surface reactions (Equations (1) and (2) in Section 2.2). Detailed deposition mechanisms for the different oxides, involving $Al_2O_3$, ZnO and $ZrO_2$, can be found in our previous work [12,36–40]. As a result, ultrathin oxide coatings under ALD growth always reveal desirable conformality, uniformity, robustness, and pinhole-free features. Furthermore, thickness of the resultant oxide coatings can be precisely controlled at the Angstrom or atomic monolayer level, which is determined by the number of ALD cycles. Accordingly, morphologic and structural differences of pristine NCM811, 20 $Al_2O_3$ ALD NCM811, and 50 $Al_2O_3$ ALD NCM811 materials are compared in Figure 1b–j. The pristine NCM811 material (Figure 1b) reveals a distinct aggregation of tremendous primary nanoparticles, which have smooth facets and sharp edges with an average particle size of ~500 nm. Such morphologic features generally indicate the high crystallinity and purity of the prepared NCM811 particles. By contrast, FESEM images of the 20 $Al_2O_3$ ALD NCM811 particles showed apparent roughness at the entire surface after coating the $Al_2O_3$ layer in 20 ALD cycles (Figure 1c), implying the conformal and uniform surface modification of the NCM811 substrate. The elemental energy dispersive spectroscopic (EDS) mapping was captured on the selected 20 $Al_2O_3$ ALD NCM811 particles (Figure 1d), which revealed even distributions of Al, Ni, Co, Mn, and O elements, and thus again demonstrated desirable conformality and uniformity of $Al_2O_3$ coatings at the surface of NCM811 particles. In order to comprehensively understand structural characteristics of the resultant $Al_2O_3$ layer, 50 $Al_2O_3$ ALD NCM811 particles with increased coating thickness were examined by TEM observations, and compared to bare NCM811 and the 20 $Al_2O_3$ ALD NCM811 materials. As shown in Figure 1e, TEM images of NCM811 particles showed consistent contrast throughout the whole observation area, revealing a single solid structure without any surface modifications. HRTEM images of the selected region in Figure 1e, marked by a blue square, showed perfect lattice fringes with a d-space of 0.47 nm (Figure 1h), corresponding to (003) planes in the layered structure of NCM811 oxide. By contrast, TEM images of the 20 $Al_2O_3$ ALD NCM811 and 50 $Al_2O_3$ ALD NCM811 particles captured in Figure 1f,g gave rise to distinct contrast differences between the dark NCM811 core and light $Al_2O_3$ coating shells at the surface, respectively. It was noticeable that the ALD coating contributed to satisfactory uniformity and conformality of the resultant $Al_2O_3$ layer, which was in accordance with that coated at the surface of different cathode materials reported in the literature [36,38]. The precise thickness was 5.6 nm as shown in the HRTEM image of the 50 $Al_2O_3$ ALD NCM811 (Figure 1j), corresponding to an $Al_2O_3$ ALD growth rate of 1.12 Å/cycle. Accordingly, 20 ALD cycles resulted in an $Al_2O_3$ coating with 2.2 nm thickness as shown in Figure 1i for the 20 $Al_2O_3$ ALD NCM811 materials. Furthermore, these two HRTEM observations indicated an amorphous feature of the $Al_2O_3$ coating layer, which was distinguishable from the internal crystalline NCM811 particles. As a result, SEM and TEM images demonstrated the conformational and uniform coating of the $Al_2O_3$ layer for the surface modification of Ni-rich NCM811 particles through ALD processes, together with thickness control at the sub-nano level.

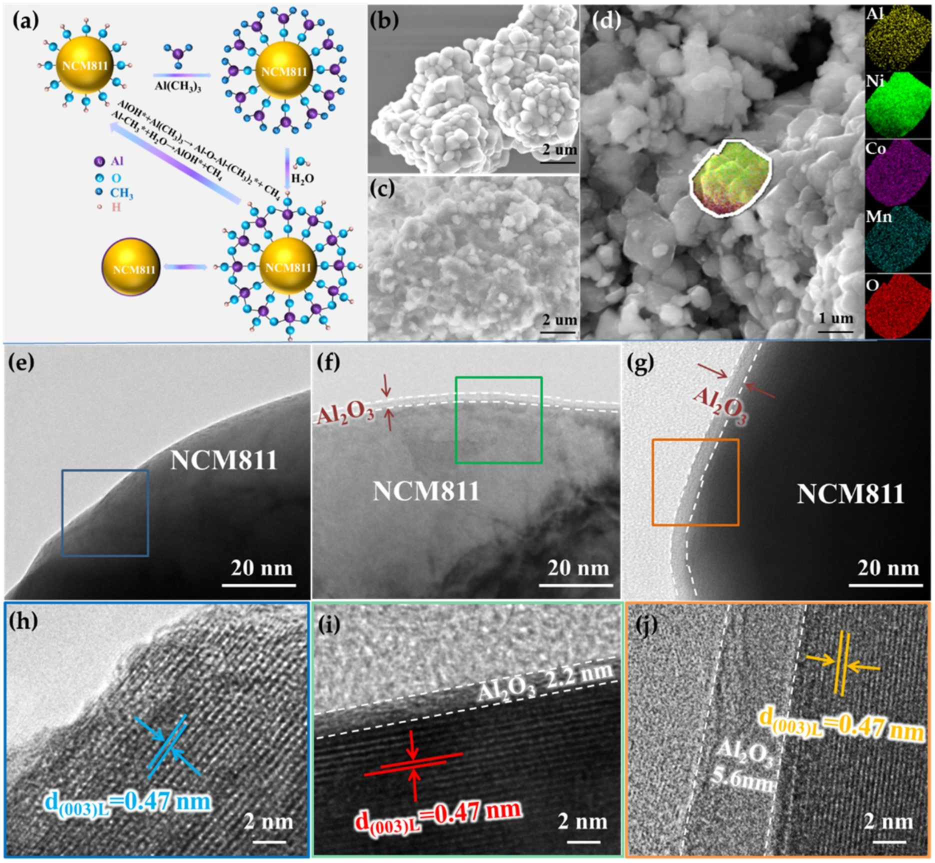

**Figure 1.** (**a**) Schematics illustration of the $Al_2O_3$ ALD growth at the surface of NCM811 particles; FESEM images of (**b**) bare NCM811, and (**c**) 20 $Al_2O_3$ ALD NCM811; EDS mapping of (**d**) 20 $Al_2O_3$ ALD NCM811; TEM images of (**e**) bare NCM811, (**f**) 20 $Al_2O_3$ ALD NCM811, and (**g**) 50 $Al_2O_3$ ALD NCM811; and HRTEM images of (**h**) bare NCM811, (**i**) 20 $Al_2O_3$ ALD NCM811, and (**j**) 50 $Al_2O_3$ ALD NCM811.

$Al_2O_3$ coating effects on changing the crystal structure of Ni-rich NCM811 core were evaluated using XRD patterns of different coated materials, coupled with quantitative analyses from Rietveld refinements. As shown in Figure 2a, the XRD pattern of pristine NCM811 material was well indexed to a layered $\alpha$-$NaFeO_2$ structure with a R-3m space group (JCPDS No. 74-0919). It also showed a desirable intensity ratio of characteristic 003 over 104 reflections, i.e., $I_{003}/I_{104}$ = 1.48 and distinct peak splitting of two 006/102 and 108/110 doublets, indicating outstanding structural ordering of the layered NCM811 material. The Rietveld refinement on the XRD pattern of pristine NCM811 resulted in lattice parameters of $a$ = 2.8746 Å, $c$ = 14.2102 Å, and $V$ = 101.72 Å$^3$, together with a low estimated $Li^+/Ni^{2+}$ cation mixing of 3.68% based on a low reliability-factor of $R_{wp}$ = 6.62% (Table 1). These XRD features all indicate an excellent layered structure of the prepared Ni-rich NCM811 material, in accordance with HRTEM images (Figure 1h). XRD patterns and the associated refinement results of NCM811 particles coated with 10, 20, and 50 $Al_2O_3$ ALD layers are displayed in Figure 2b–d, respectively. The calculated lattice parameters and cation mixings of these three coated materials, with gradually-increasing coating thickness of $Al_2O_3$, are summarized in Table 1 compared to bare NCM811, together with values of standard deviations (s.d.) for the calculations. The $Al_2O_3$ phase was not detectable even in the 50 $Al_2O_3$ ALD NCM811 samples, owing to the amorphous phase. However, the $Al_2O_3$ coating slightly suppressed the crystal structural of the internal NCM811 host. Coatings thicker than 2 nm, i.e., 20 ALD cycles (20 cycle* 1.12 Å/cycle = 2.24 nm), resulted in a detectable decrease in $a$, $c$, and $V$ values, according to the refinement results of the 20 $Al_2O_3$ ALD NCM811 sample, while the 10 $Al_2O_3$ ALD NCM811 showed little change in lattice parameters as compared with that in the pristine NCM811 (Table 1). Although the thick $Al_2O_3$ coating reduced $a$ and $c$ values of the 50 $Al_2O_3$ ALD NCM811 material, its $c/a$ ratio was almost the same with the NCM811, again indicating high conformality and uniformity of surface modifications via oxide ALD coatings. On the other hand, XRD patterns of the three $Al_2O_3$-coated NCM811 materials revealed $I_{003}/I_{104}$ values equal to 1.54, 1.46, and 1.45 after 10, 20, and 50 ALD cycles (Figure 2b–d), respectively, indicating little effects of $Al_2O_3$ ALD coating on the structural ordering of internal NCM811 material. The estimated cation mixings within the layered structures of these three samples wre all in an acceptable range of 3%–4%, consistent with that of the pristine NCM811 material (Table 1).

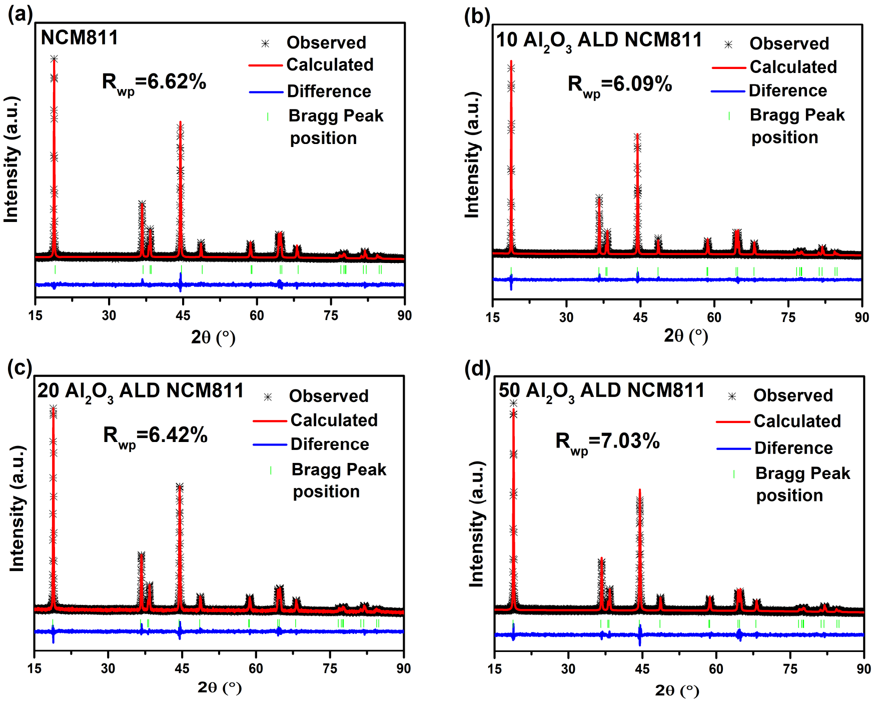

**Figure 2.** XRD patterns of (**a**) bare NCM8111; (**b**) 10 $Al_2O_3$ ALD NCM8111; (**c**) 20 $Al_2O_3$ ALD NCM8111; and (**d**) 50 $Al_2O_3$ ALD NCM8111 materials, coupled with rietveld refinement results.

**Table 1.** Crystal parameters of different $Al_2O_3$-coated NCM811 materials in comparison to bare NCM811, according to XRD patterns and refinement results as shown in Figure 2.

| Samples | $a$ (Å) | s.d. | $c$ (Å) | s.d. | Volume (Å$^3$) | s.d. | $c/a$ | Li$^+$ at 3$b$ Sites | s.d. | $R_{wp}$ (%) | $R_p$ (%) |
|---|---|---|---|---|---|---|---|---|---|---|---|
| NCM811 | 2.8746 | $3 \times 10^{-5}$ | 14.2102 | $1.8 \times 10^{-3}$ | 101.72 | $2.87 \times 10^{-3}$ | 4.9432 | 0.9632 | $2.203 \times 10^{-3}$ | 6.62 | 4.81 |
| 10 $Al_2O_3$ ALD NCM811 | 2.8745 | $3 \times 10^{-5}$ | 14.2095 | $3.1 \times 10^{-3}$ | 101.71 | $3.1 \times 10^{-3}$ | 4.9433 | 0.9634 | $2.351 \times 10^{-3}$ | 6.09 | 5.12 |
| 20 $Al_2O_3$ ALD NCM811 | 2.8743 | $2 \times 10^{-5}$ | 14.2094 | $3.6 \times 10^{-3}$ | 101.65 | $3.05 \times 10^{-3}$ | 4.9436 | 0.9697 | $1.936 \times 10^{-3}$ | 6.42 | 5.18 |
| 50 $Al_2O_3$ ALD NCM811 | 2.8739 | $4 \times 10^{-5}$ | 14.2071 | $5.2 \times 10^{-3}$ | 101.49 | $7.93 \times 10^{-3}$ | 4.9435 | 0.9666 | $7.725 \times 10^{-3}$ | 7.03 | 5.58 |

In order to confirm $Al_2O_3$ coating formation and its possible impacts on the chemical environments of transition metal cations at the surface of NCM811 particles, characteristic Al 2*p*, Ni 2*p*, Co 2*p*, and Mn 2*p* XPS peaks of bare NCM811 and three $Al_2O_3$-coated NCM811 materials were measured and compared. As shown in Figure 3a, 10 $Al_2O_3$ ALD NCM811, 20 $Al_2O_3$ ALD NCM811, and 50 $Al_2O_3$ ALD NCM811 samples all showed sharp Al 2*p* XPS peaks, verifying successful $Al_2O_3$ coating at the surface of NCM811 particles. These collected Al 2*p* peaks slightly shifted to higher binding energies at 75.4, 75.6, and 75.7 eV, respectively, compared to 74.6 eV of pure $Al_2O_3$ oxide reported in NIST XPS Database, implying possible chemical bonding between the $Al_2O_3$ coating layer and NCM811 particles. As reported in the literature [36–40], the oxide coating and substrate in a typical ALD growth can result in a favorable chemical bond of substrate–O–$M_xO_y$ (M = Al, Zn, Zr, Sn, etc.), this process is illustrated in Figure 1a. However, it is unexpected to see that all the characteristic of Ni 2*p*, Co 2*p*, and Mn 2*p* XPS peaks captured on three $Al_2O_3$-coated NCM811 particles also gave rise to higher bonding energies compared to those of pristine NCM811 particles, when the coating thickness of $Al_2O_3$ was gradually increased (Figure 3b–d). These interesting XPS results may be attributed to the tremendous –OH groups that were left at the surface of $Al_2O_3$ coating at the end of ALD growth (Figure 1a), which are highly electronegative, and thus probably induce reduced electron cloud densities of Al, Ni, Co, and Mn cations. The thicker $Al_2O_3$ coating resulted in increased surface area of $Al_2O_3$-coated NCM811 particles as well as the quantity of residual –OH groups at the most outside surface; hence, the inductive effect was enhanced by the increased number of –OH groups, leading to binding energy shifts of different cations to higher values. XPS results indicate a probable chemical bonding between $Al_2O_3$ and NCM811, which may facilitate charge transfer and lithium ion diffusion through the oxide coating layer.

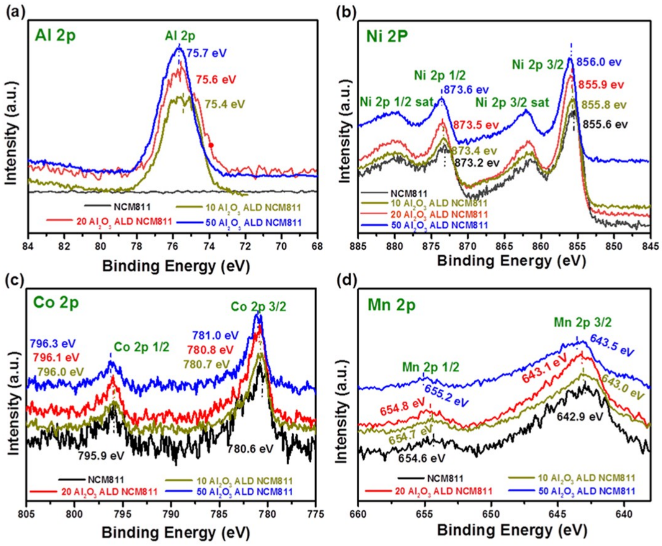

**Figure 3.** Characteristics XPS spectra captured on the 10 $Al_2O_3$ ALD NCM811, 20 $Al_2O_3$ ALD NCM811, and 50 $Al_2O_3$ ALD NCM811 materials compared to the bare NCM811: (**a**) Al 2*p*, (**b**) Ni 2*p*, (**c**) Co 2*p*, and (**d**) Mn 2*p* peaks.

### *3.2. Enhanced Electrochemical Performance of Ni-Rich NCM811 Cathode Materials by $Al_2O_3$ ALD Coating*

Effects of $Al_2O_3$ ALD coating on improving electrochemical performance of Ni-rich NCM811 cathode material are evaluated in Figure 4, where different cathode materials were subjected to a broad voltage range of 2.7–4.6 V vs. $Li^+/Li$. Figure 4a compares resultant cycling performance of the $Al_2O_3$-coated NCM811 cycled at 0.1 C with bare NCM811 material. The coating thickness of $Al_2O_3$ layer was optimized at ~2 nm, corresponding to 20 ALD cycles. As a result, the 20 $Al_2O_3$ ALD NCM811 cathode delivered an impressive discharge capacity of 212.8 mAh/g and an associated initial columbic efficiency of 84.0% in the first cycle, which were both higher than 198.2 mAh/g and 76.1% of the pristine NCM811 without $Al_2O_3$ protection. Accordingly, the charge/discharge curves of these two cathode materials cycled at 1st and 100th cycles are shown in Figure 4b. The improved electrochemical reversibility with increased specific capacity of the 20 $Al_2O_3$ ALD NCM811 in the first cycle can be attributed to the conformal surface modification from the $Al_2O_3$ coating (Figure 1a), which effectively suppressed detrimental side reactions even when the NCM811 cathode material was cycled in an extended voltage range up to 4.6 V. In addition to protecting the internal Ni-rich core material from the HF attack in electrolytes as reported in the literature [29,41], the conformational and uniform $Al_2O_3$ coating also reduced the electrolyte decomposition induced by high oxidation of $Ni^{3+}/Ni^{4+}$ redox, especially under the deeply-charged condition at a high cut-off voltage of 4.6 V. As shown in Figure 4a,b, the pristine NCM811 cathode material suffered from distinct capacity decay to 127.5 mAh/g after 100 electrochemical cycles, while the 20 $Al_2O_3$ ALD NCM811 retained a much higher capacity of 157.2 mAh/g in the 100th cycle. Furthermore, the NCM811 also encountered an obvious working voltage fading from 3.80 initially to 3.76 V in the 100th cycle. By contrast, electrochemical polarity was effectively inhibited in the 20 $Al_2O_3$ ALD NCM811 cathode material, resulting in a well-preserved working voltage from 3.84 V in the first cycle to 3.83 V after 100 cycles. The 10 $Al_2O_3$ ALD NCM811 delivered moderate cycling performance as shown in Figure 4a, between the NCM811 and 20 $Al_2O_3$ ALD NCM811, which was attributed to the thinner $Al_2O_3$ coating around 1 nm. On the other hand, the much thicker coating of $Al_2O_3$ layer (>5 nm) after 50 ALD cycles resulted in satisfactory cycling stability, but the lithium storage capacity had to be sacrificed (Figure 4a), owing to the inferior conductivity of insulating $Al_2O_3$ oxide [42,43]. According to reports in the literature [13,44], Ni-rich cathode materials undergo inevitable phase transitions among three hexagonal (H1, H2, and H3) and one monoclinic (M) phases in their layered structures during lithiation/delithiation, which further aggravate undesired capacity fading in long-term electrochemical cycles. In order to examine possible phase transitions, related differential capacity ($dQ/dV$) profiles are shown in Figure 4c, which were transferred from charge/discharge curves in Figure 4b. The initial anodic peak of pristine NCM811 showed the much higher intensity by contrast with 20 $Al_2O_3$ ALD NCM811, indicating severe parasitic side reactions that occurred during the first phase transformation from the hexagonal H1 to monoclinic M phases. Subsequent M to H2, and H2 to H3 took place around at 4.0 and 4.2 V as marked in Figure 4c, respectively, when the Ni-rich cathode materials were charged to a high cutoff voltage. In successive discharge processes, phase transitions from H3 to H2 to M were reduced, resulting in dominant cathodic peaks around 3.75 V both in NCM811 and 20 $Al_2O_3$ ALD NCM811 cathodes. However, two redox pairs at higher voltages around 4.0 and 4.2 V were detected in the 100th cycle of pristine NCM811 cathode (peak voltages of detected anodic and cathodic peaks are marked by underlines), while the 20 $Al_2O_3$ ALD NCM811 gave rise to the smoother $dQ/dV$ curves above 3.9 V, revealing significantly suppressed phase transitions for its enhanced cycling stability after the optimal $Al_2O_3$ ALD coating. Furthermore, total resistance changes of these two cathodes after 100 cycles were determined by EIS spectra as shown in Figure 4d. These measurements were conducted on their fully-discharged states after prolonged electrochemical cycles. EIS spectra of fresh cells were also recorded at open circuit voltage states for the comparison. It is worth noting that two fresh cells of NCM811 and the 20 $Al_2O_3$ ALD NCM811 cathodes both showed small resistances around 25 Ω. However, two Nyquist circles with larger diameters were captured in both cathodes after 100 cycles. The selected equivalent circuit, as the inset, was used to calculate the associated resistances based on fitting solid lines. For the pristine NCM811, one Nyquist circle in high frequency may be attributed to impure phases, such as spinel-like and/or rock-salt phases formed during prolonged cycles as reported in the literature [45,46], and others in low frequency were assigned to the solid electrolyte interphase (SEI) film. By contrast, two Nyquist circles in 20 $Al_2O_3$ ALD NCM811 resulted from the $Al_2O_3$ coating and SEI film at the surface of cycled cathode material, respectively. It is noticeable that introduction of 2 nm $Al_2O_3$ coating led to acceptable resistance at 29 Ω, which was smaller than the 35 Ω caused by the secondary impure structure that formed at the surface of NCM811 without surface modification. Moreover, the 20 $Al_2O_3$ ALD NCM811 resulted in considerable decrease (160 Ω) corresponding to SEI film resistance, while the pristine NCM811 brought about larger SEI resistance (250 Ω). Electrochemical performance demonstrated significant effects of the optimized $Al_2O_3$ ALD coating on reducing electrochemical polarity and improving reversibility of Ni-rich cathode materials for superior lithium ion batteries.

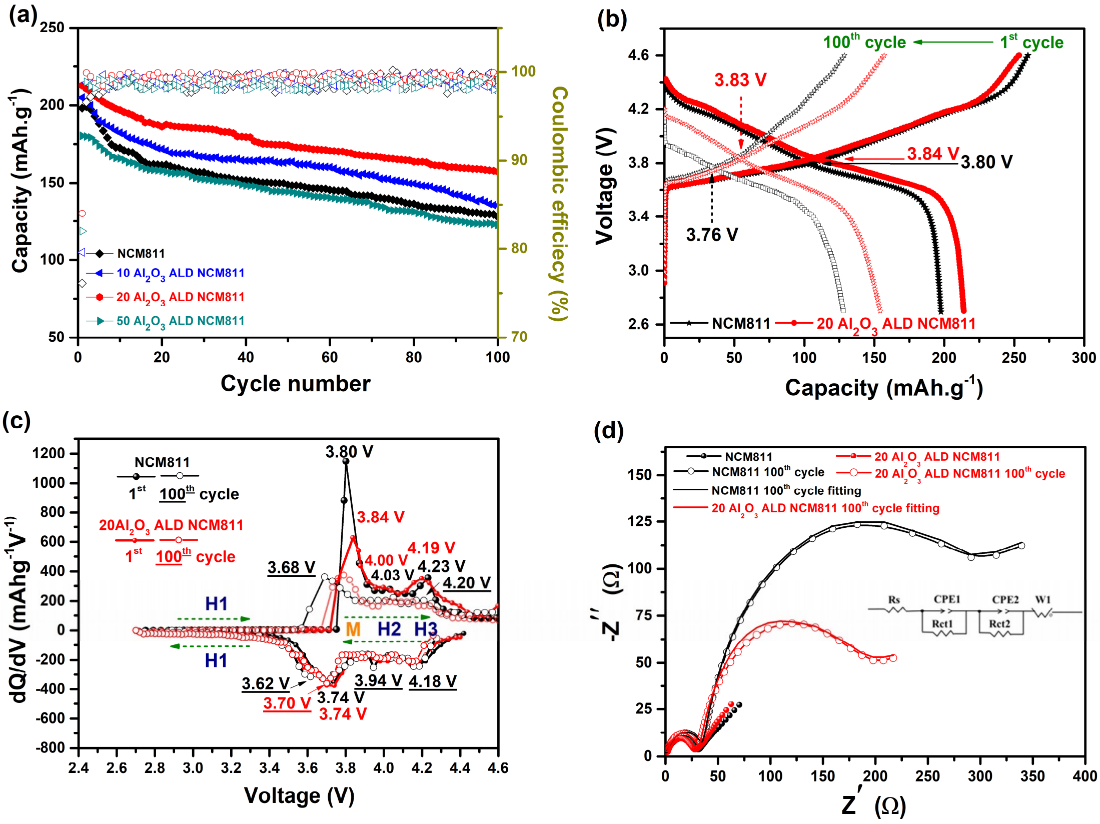

**Figure 4.** Electrochemical performance of different cathode materials in a broad voltage range of 2.7–4.6 V vs. $Li^+$/Li: (**a**) cycling performance at 0.1 C for 100 cycles; (**b**) charge/discharge curves of bare NCM811 and 20 $Al_2O_3$ ALD NCM811 in the first and 100th cycles at 0.1 C; (**c**) d*Q*/d*V* profiles of bare NCM811 and 20 $Al_2O_3$ ALD NCM811 in the first and 100th cycles; and (**d**) EIS spectra captured on fresh cells (solid patterns) at open circuit voltage states and after 100 cycles at fully-discharged states (hollow patterns).

## 4. Conclusions

Enhanced cycling stability of Ni-rich $LiNi_{0.8}Co_{0.1}Mn_{0.1}O_2$ cathode material in an extended voltage range has been realized by surface modification of ultrathin $Al_2O_3$ coating through atomic layer deposition. The oxide ALD growth leads to impressive conformality and uniformity of resultant $Al_2O_3$ layer, and the coating thickness can be precisely controlled at 1.12 Å per ALD cycle. The optimal thickness of the $Al_2O_3$ coating for $LiNi_{0.8}Co_{0.1}Mn_{0.1}O_2$ cathode material is in 2 nm level through performing 20 ALD cycles. Either the thicker or thinner coating thickness leads to decreased lithium storage capacity together with inferior cycling performance of different $Al_2O_3$

coated $LiNi_{0.8}Co_{0.1}Mn_{0.1}O_2$ cathodes. The optimized 20 $Al_2O_3$ ALD modified $LiNi_{0.8}Co_{0.1}Mn_{0.1}O_2$ cathode material distinctly shows increased discharge capacity and columbic efficiency in the first cycle, as well as improved capacity retention after successive 100 cycles in comparison with the pristine material. Electrochemical features in the first and 100th cycle of cathode materials, with and without $Al_2O_3$ protection were compared, involving charge/discharge curves, differential capacity profiles, and electrochemical impedance spectra. The $Al_2O_3$ coating has been demonstrated to suppress parasitic side reactions and phase transitions during prolonged lithiation/delithiation of the $LiNi_{0.8}Co_{0.1}Mn_{0.1}O_2$ cathode, resulting in reduced electrochemical polarity and enhanced cycling stability for Ni-rich cathode materials cycled in broad voltage ranges.

**Author Contributions:** Conceptualization, J.Z.; Methodology, W.Z., T.L., Z.X., and X.H.; Software, L.B.; Data Curation, W.Z., X.H., L.B., and K.T.; Writing—Original Draft Preparation, W.Z.; Writing—Review and Editing, Y.W., H.W., J.Z., and L.G.; Project Administration, L.G. and J.Z.; Funding Acquisition, L.G. and J.Z.

**Funding:** This research was funded by the National Natural Science Foundation of China (Nos. 21703147 and U1401248); the Jiangsu Provincial Natural Science Foundations for the Young Scientist (No. BK20170338); the General Financial Grant from the China Postdoctoral Science Foundation (No. 2016M601876); and the Open Fund of Jiangsu Key Laboratory of Materials and Technology for Energy Conversion (No. MTEC-2017M01).

**Acknowledgments:** The authors acknowledge Suzhou Key Laboratory for the Advanced Carbon Materials and Wearable Energy Technologies, Suzhou 215006, China.

**Conflicts of Interest:** The authors declare no conflicts of interest.

## References

1. Poizot, P.; Laruelle, S.; Grugeon, S.; Grugeon, L.; Tarascon, J.M. Nano-sized transition-metal oxides as negative-electrode materials for Lithium-ion batteries. *Nature* **2000**, *407*, 496–499. [CrossRef]
2. Mizushima, K.; Jones, P.C.; Wiseman, P.J.; Goodenough, J.B. $Li_xCoO_2$ ($0 < x < -1$): A new cathode material for batteries of high energy density. *Mater. Res. Bull.* **1980**, *15*, 783–789. [CrossRef]
3. Thackeray, M.M.; Wolverton, C.; Isaacs, E.D. Electrical energy storage for transportation-approaching the limits of, and going beyond, Lithium-ion batteries. *Energy Environ. Sci.* **2012**, *5*, 7854–7863. [CrossRef]
4. Tang, Y.; Deng, J.; Li, W.; Malyi, O.I.; Zhang, Y.; Zhou, X.; Pan, S.; Wei, J.; Cai, Y.; Chen, Z. Water-soluble sericin protein enabling stable solid-electrolyte interphase for fast charging high voltage battery electrode. *Adv. Mater.* **2017**, *29*, 1701828. [CrossRef]
5. Tang, Y.; Zhang, Y.; Malyi, O.I.; Bucher, N.; Xia, H.; Xi, S.; Zhu, Z.; Lv, Z.; Li, W.; Wei, J. Identifying the origin and contribution of surface storage in $TiO_2$(B) nanotube electrode by in situ dynamic valence state monitoring. *Adv. Mater.* **2018**, *36*, 1802200. [CrossRef]
6. Zhang, Y.; Malyi, O.I.; Tang, Y.; Wei, J.; Zhu, Z.; Xia, H.; Li, W.; Guo, J.; Zhou, X.; Chen, Z. Reducing the charge carrier transport barrier in functionally layer-graded electrodes. *Angew. Chem.* **2017**, *56*, 14847. [CrossRef]
7. Yi, R.; Dai, F.; Gordin, M.L.; Chen, S.; Wang, D. Lithium-ion batteries: micro-sized Si–C composite with interconnected nanoscale building blocks as high-performance anodes for practical application in Lithium-ion batteries. *Adv. Energy Mater.* **2013**, *3*, 273. [CrossRef]
8. Fergus, J.W. Recent developments in cathode materials for Lithium ion batteries. *J. Power Sources* **2010**, *195*, 939–954. [CrossRef]
9. Lee, J.; Kitchaev, D.A.; Kwon, D.H.; Lee, C.W.; Papp, J.K.; Liu, Y.S.; Lun, Z.; Clément, R.J.; Shi, T.; Mccloskey, B.D. Reversible $Mn^{2+}/Mn^{4+}$ double redox in Lithium-excess cathode materials. *Nature* **2018**, *556*, 185–190. [CrossRef]
10. Jiang, K.C.; Wu, X.L.; Yin, Y.X.; Lee, J.S.; Kim, J.; Guo, Y.G. Superior hybrid cathode material containing Lithium-excess layered material and graphene for Lithium-ion Batteries. *ACS Appl. Mater. Interfaces* **2012**, *4*, 4858–4863. [CrossRef]
11. Zhao, J.; Zhang, W.; Huq, A.; Misture, S.T.; Zhang, B.; Guo, S.; Wu, L.; Zhu, Y.; Chen, Z.; Amine, K. In situ probing and synthetic control of cationic ordering in Ni-Rich layered oxide cathodes. *Adv. Energy Mater.* **2017**, *7*, 1601266. [CrossRef]
12. Zhao, J.; Aziz, S.; Wang, Y. Hierarchical functional layers on high-capacity Lithium-excess cathodes for superior Lithium ion batteries. *J. Power Sources* **2014**, *247*, 95–104. [CrossRef]

13. Zhao, J.; Huang, R.; Gao, W.; Zuo, J.M.; Zhang, X.F.; Misture, S.T.; Chen, Y.; Lockard, J.V.; Zhang, B.; Guo, S. An Ion-exchange promoted phase transition in a Li-excess layered cathode material for high-performance Lithium ion batteries. *Adv. Energy Mater.* **2015**, *5*, 1401937. [CrossRef]
14. Martha, S.K.; Sclar, H.; Framowitz, Z.S.; Kovacheva, D.; Saliyski, N.; Gofer, Y.; Sharon, P.; Golik, E.; Markovsky, B.; Aurbach, D. A comparative study of electrodes comprising nanometric and submicron particles of $LiNi_{0.5}Mn_{0.5}O_2$, $LiNi_{0.33}Mn_{0.33}Co_{0.33}O_2$, and $LiNi_{0.4}Mn_{0.4}Co_{0.2}O_2$ layered compounds. *J. Power Sources* **2009**, *189*, 248–255. [CrossRef]
15. Li, X.; Cheng, F.; Guo, B.; Chen, J. Template-synthesized $LiCoO_2$, $LiMn_2O_4$, and $LiNi_{0.8}Co_{0.2}O_2$ nanotubes as the cathode materials of Lithium ion batteries. *J. Phys. Chem. B* **2005**, *109*, 14017–14024. [CrossRef]
16. Liu, W.; Oh, P.; Liu, X.; Lee, M.J.; Cho, W.; Chae, S.; Kim, Y.; Cho, J. Nickel-rich layered Lithium transition-metal oxide for high-energy Lithium-ion batteries. *Angew. Chem.* **2015**, *54*, 4440–4457. [CrossRef]
17. Zhong, S.; Lai, M.; Yao, W.; Li, Z. Synthesis and electrochemical properties of $LiNi_{0.8}Co_xMn_{0.2-x}O_2$ positive-electrode material for Lithium-ion batteries. *Electrochim. Acta* **2016**, *212*, 343–351. [CrossRef]
18. Zou, Y.; Yang, X.; Lv, C.; Liu, T.; Xia, Y.; Shang, L.; Waterhouse, G.I.; Yang, D.; Zhang, T. Multishelled Ni-Rich $Li(Ni_xCo_yMn_z)O_2$ hollow fibers with low cation mixing as high-performance cathode materials for Li-ion batteries. *Adv. Sci.* **2017**, *4*, 1600262. [CrossRef]
19. Zhang, X.; Jiang, W.J.; Mauger, A.; QILU; Gendron, F.; Julien, C.M. Minimization of the cation mixing in $Li_{1+x}(NMC)_{1-x}O_2$ as cathode material. *J. Power Sources* **2009**, *195*, 1292–1301. [CrossRef]
20. Manthiram, A.; Song, B.; Li, W. A perspective on nickel-rich layered oxide cathodes for Lithium-ion batteries. *Energy Storage Mater.* **2017**, *6*, 125–139. [CrossRef]
21. Zheng, J.; Kan, W.H.; Manthiram, A. Role of Mn content on the electrochemical properties of nickel-rich layered $LiNi_{(0.8-x)}Co_{(0.1)}Mn_{(0.1+x)}O_2$ ($0.0 \leq x \leq 0.08$) cathodes for lithium-ion batteries. *ACS Appl. Mater. Interfaces* **2015**, *7*, 6926–6934. [CrossRef]
22. Oh, P.; Oh, S.M.; Li, W.; Myeong, S.; Cho, J.; Manthiram, A. High-performance heterostructured cathodes for Lithium-ion batteries with a Ni-rich layered oxide core and a Li-rich layered oxide shell. *Adv. Sci.* **2016**, *3*, 1600184. [CrossRef]
23. Song, B. A facile cathode design combining Ni-rich layered oxides with Li-rich layered oxides for Lithium-ion batteries. *J. Power Sources* **2016**, *325*, 620–629. [CrossRef]
24. Schipper, F.; Bouzaglo, H.; Dixit, M.; Erickson, E.M.; Weigel, T.; Talianker, M.; Grinblat, J.; Burstein, L.; Schmidt, M.; Lampert, J. From surface $ZrO_2$ coating to bulk Zr doping by high temperature annealing of nickel-rich lithiated oxides and their enhanced electrochemical performance in Lithium ion batteries. *Adv. Energy Mater.* **2018**, *8*, 1701682. [CrossRef]
25. Tan, L.; Liu, H. Influence of ZnO coating on the structure, morphology and electrochemical performances for $LiNi_{1/3}Co_{1/3}Mn_{1/3}O_2$ material. *Russ. J. Electrochem.* **2011**, *47*, 156–160. [CrossRef]
26. Li, J.; Fan, M.; He, X.; Zhao, R.; Jiange, C.; Wan, C. $TiO_2$ coating of $LiNi_{1/3}Co_{1/3}Mn_{1/3}O_2$ cathode materials for Li-ion batteries. *Ionics* **2006**, *12*, 215–218. [CrossRef]
27. Cheng, C.; Yi, H.; Chen, F. Effect of $Cr_2O_3$ Coating on $LiNi_{1/3}Co_{1/3}Mn_{1/3}O_2$ as cathode for Lithium-ion batteries. *J. Electron. Mater.* **2014**, *43*, 3681–3687. [CrossRef]
28. Hudaya, C.; Ji, H.P.; Lee, J.K.; Choi, W. $SnO_2$-coated $LiCoO_2$ cathode material for high-voltage applications in Lithium-ion batteries. *Solid State Ionics* **2014**, *256*, 89–92. [CrossRef]
29. Li, X.; Liu, J.; Meng, X.; Tang, Y.; Banis, M.N.; Yang, J.; Hu, Y.; Li, R.; Cai, M.; Sun, X. Significant impact on cathode performance of Lithium-ion batteries by precisely controlled metal oxide nanocoatings via atomic layer deposition. *J. Power Sources* **2014**, *247*, 57–69. [CrossRef]
30. Wang, Z.; Liu, L.; Chen, L.; Huang, X. Structural and electrochemical characterizations of surface-modified $LiCoO_2$ cathode materials for Li-ion batteries. *Solid State Ionics* **2002**, *148*, 335–342. [CrossRef]
31. Kim, J.W.; Kim, D.H.; Oh, D.Y.; Lee, H.; Kim, J.H.; Lee, J.H.; Jung, Y.S. Surface chemistry of $LiNi_{0.5}Mn_{1.5}O_4$ particles coated by $Al_2O_3$ using atomic layer deposition for Lithium-ion batteries. *J. Power Sources* **2015**, *274*, 1254–1262. [CrossRef]
32. Guan, D.; Wang, Y. Ultrathin surface coatings to enhance cycling stability of $LiMn_2O_4$ cathode in Lithium-ion batteries. *Ionics* **2013**, *19*, 1–8. [CrossRef]
33. Mohanty, D.; Dahlberg, K.; King, D.M.; David, L.A.; Sefat, A.S.; Wood, D.L.; Daniel, C.; Dhar, S.; Mahajan, V.; Lee, M. Modification of Ni-rich FCG NMC and NCA cathodes by atomic layer deposition: preventing surface phase transitions for high-voltage Lithium-ion batteries. *Sci. Rep.* **2016**, *6*, 26532. [CrossRef]

34. Shi, Y.; Zhang, M.; Qian, D.; Meng, Y.S. Ultrathin $Al_2O_3$ coatings for improved cycling performance and thermal stability of $LiNi_{0.5}Co_{0.2}Mn_{0.3}O_2$ cathode material. *Electrochim. Acta* **2016**, *203*, 154–161. [CrossRef]
35. Zhang, X.; Belharouak, I.; Li, L.; Lei, Y.; Elam, J.W.; Nie, A.; Chen, X.; Yassar, R.S.; Axelbaum, R.L. Structural and electrochemical study of $Al_2O_3$ and $TiO_2$ Coated $Li_{1.2}Ni_{0.13}Mn_{0.54}Co_{0.13}O_2$ cathode material using ALD. *Adv. Energy Mater.* **2013**, *3*, 1299–1307. [CrossRef]
36. Zhao, J.; Wang, Y. Atomic layer deposition of epitaxial $ZrO_2$ coating on $LiMn_2O_4$ nanoparticles for high-rate lithium ion batteries at elevated temperature. *Nano Energy* **2013**, *2*, 882–889. [CrossRef]
37. Aziz, S.; Zhao, J.; Cain, C.; Wang, Y. Nanoarchitectured $LiMn_2O_4$/Graphene/ZnO composites as electrodes for Lithium ion batteries. *J. Mater. Sci. Technol.* **2014**, *30*, 427–433. [CrossRef]
38. Zhao, J.; Wang, Y. Surface modifications of Li-ion battery electrodes with various ultrathin amphoteric oxide coatings for enhanced cycleability. *J. Solid State Electrochem.* **2013**, *17*, 1049–1058. [CrossRef]
39. Zhao, J.; Ying, W. Ultrathin surface coatings for improved electrochemical performance of Lithium ion battery electrodes at elevated temperature. *J. Phys. Chem. C* **2012**, *116*, 11867–11876. [CrossRef]
40. Zhao, J.; Wang, Y. High-capacity full Lithium-ion cells based on nanoarchitectured ternary manganese-nickel-cobalt carbonate and its lithiated derivative. *J. Mater. Chem. A* **2014**, *2*, 14947–14956. [CrossRef]
41. Aykol, M.; Kirklin, S.; Wolverton, C. Thermodynamic aspects of cathode coatings for Lithium-ion batteries. *Adv. Energy Mater.* **2015**, *4*, 1400690. [CrossRef]
42. Zhao, F.; Tang, Y.; Wang, J.; Tian, J.; Ge, H.; Wang, B. Vapor-assisted synthesis of $Al_2O_3$-coated $LiCoO_2$ for high-voltage lithium ion batteries. *Electrochim. Acta* **2015**, *174*, 384–390. [CrossRef]
43. Araki, K.; Taguchi, N.; Sakaebe, H.; Tatsumi, K.; Ogumi, Z. Electrochemical properties of $LiNi_{1/3}Co_{1/3}Mn_{1/3}O_2$ cathode material modified by coating with $Al_2O_3$ nanoparticles. *J. Power Sources* **2014**, *269*, 236–243. [CrossRef]
44. Kalluri, S.; Yoon, M.; Jo, M.; Liu, H.K.; Dou, S.X.; Cho, J.; Guo, Z. Feasibility of cathode surface coating technology for high-energy Lithium-ion and beyond-Lithium-ion batteries. *Adv. Mater.* **2017**, *29*, 1605807. [CrossRef]
45. Liu, S.; Xiong, L.; He, C. Long cycle life lithium ion battery with lithium nickel cobalt manganese oxide (NCM) cathode. *J. Power Sources* **2014**, *261*, 285–291. [CrossRef]
46. Jung, S.K.; Gwon, H.; Hong, J.; Park, K.Y.; Seo, D.H.; Kim, H.; Hyun, J.; Yang, W.; Kang, K. Understanding the degradation mechanisms of $LiNi_{0.5}Co_{0.2}Mn_{0.3}O_2$ cathode material in Lithium ion batteries. *Adv. Energy Mater.* **2014**, *4*, 1300787. [CrossRef]